Surface-Enhanced Raman Scattering Nanoparticles for Multiplexed Imaging of Bladder Cancer Tissue Permeability and Molecular Phenotype

*Ryan M. Davis[1], Bernhard Kiss[2,3], Dharati R. Trivedi[2,4], Thomas J. Metzner[2], Joseph C. Liao[2,4], Sanjiv S. Gambhir[1]**

[1]Department of Radiology, Stanford University, Stanford, CA, 94305, USA

[2]Department of Urology, Stanford University School of Medicine, Stanford, CA 94305, USA

[3]Institute for Stem Cell Biology and Regenerative Medicine, Stanford University, Stanford, CA 94305, USA

[4]Veterans Affairs Palo Alto Health Care System, Palo Alto, CA, 94550, USA

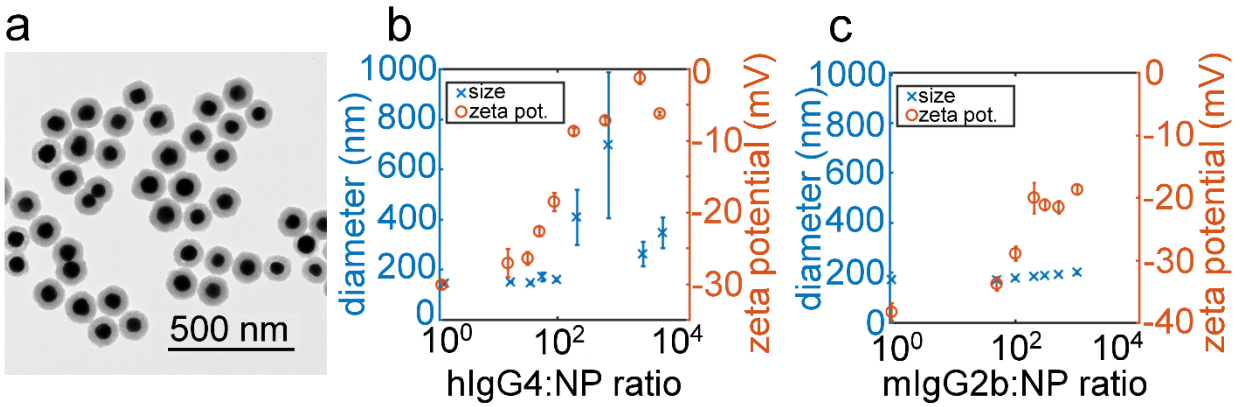

Figure S1: Physiochemical Characterization of SERS Nanoparticles with DL650 and Isotype Control Antibodies Conjugated to the Surface. a) TEM image of naked s440 nanoparticles. The dark portion is the gold and the lighter gray portion is silica. b) titration of hIgG4 isotype control antibody onto the surface of s440 SERS nanoparticles (no dye). The zeta potential and hydrodynamic radius are shown for different molar ratios of antibody and nanoparticle. c) titration of mIgG2b isotype control onto s420-DL650.

Physiochemical characterization of SERS nanoparticles

The zeta potentials of DyLight 650-antibody-SERS conjugates (Ab:NP molar ratio 200:1) capped with MM-PEG_{12} were -21±-1mV for s440-CD47, -20±-1mV for s421-IgG4, and -14±-1mV for s420-CA9. Zeta potential values are the mean and standard deviation of six measurements, and were measured at pH 7.4 in 10mM MOPS buffer. The hydrodynamic radius of antibody-SERS conjugates (Ab:NP molar ratio 200:1) capped with MM-PEG_{12} as measured by DLS were 180±2nm for s440-CD47, 174±1nm for s421-IgG4, and 176±2nm for s420-CA9. Hydrodynamic radius values are the mean and standard deviation of three measurements. All zeta potentials and hydrodynamic radius values were measured on a Zetasizer (Malvern Instruments, Malvern, United Kingdom).

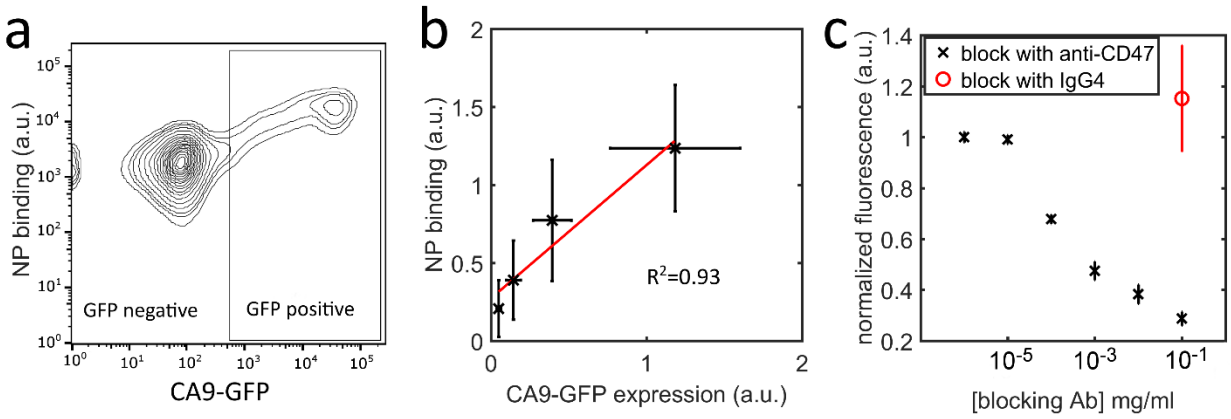

Figure S2: Binding Level of Actively-targeted Nanoparticles was Proportional to Antigen Availability in Cell Suspension. (a) Nanoparticles bound to HCT-116 cells transiently transfected with a CA9-eGFP fusion protein. As can be seen, the nanoparticle fluorescence (y-axis) increased monotonically as the CA9 expression increased. (b) Data from (a) were split into four quadrants and the nanoparticle fluorescence was plotted versus CA9-eGFP expression, indicating a strong correlation between CA9 expression and s420-CA9 binding. (c) An anti-CD47 blocking antibody was titrated on HCT-116 cells, and the bound nanoparticle fluorescence was plotted as a function of blocking antibody concentration. As can be seen, the binding of s440-CD47 decreased as the blocking antibody concentration increased.

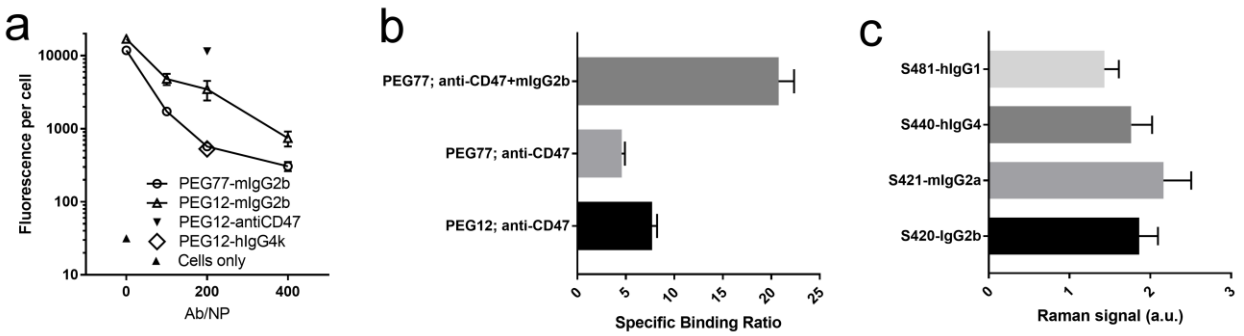

Figure S3: Nonspecific Binding of Antibody-functionalized SERS Nanoparticles in Cell Suspension and Mouse Xenograft. (a) Nonspecific binding of nanoparticles functionalized with mIgG2b or hIgG4 to HCT-116 cells in suspension. Each data point is the mean and standard deviation of the median fluorescence from three measurements. The data used NHS-$(PEG)_N$-maleimide crosslinkers of different lengths to conjugate antibodies to the nanoparticle, where N = 12 or 77. (b) Median flow cytometry fluorescence from three replicates for SERS nanoparticles actively targeted to CD47. The PEG77; anti-CD47+mIgG2b condition used NHS-$(PEG)_{77}$-maleimide to conjugate on average 200 anti-CD47 and 400 mIgG2b per nanoparticle. All means were statistically significantly different ($p<10^{-4}$). (c) nonspecific binding of different isotypes to excised HCT-116 mouse xenografts. A 1:1:1:1 mixture of s481-hIgG1, s421-mIgG2a, s440-hIgG4, and s420-IgG2b were applied to the tissue topically, washed, then imaged on a Raman endoscope. The mean binding levels of each isotype were not statistically significantly different according to the analysis of variance (ANOVA) test.

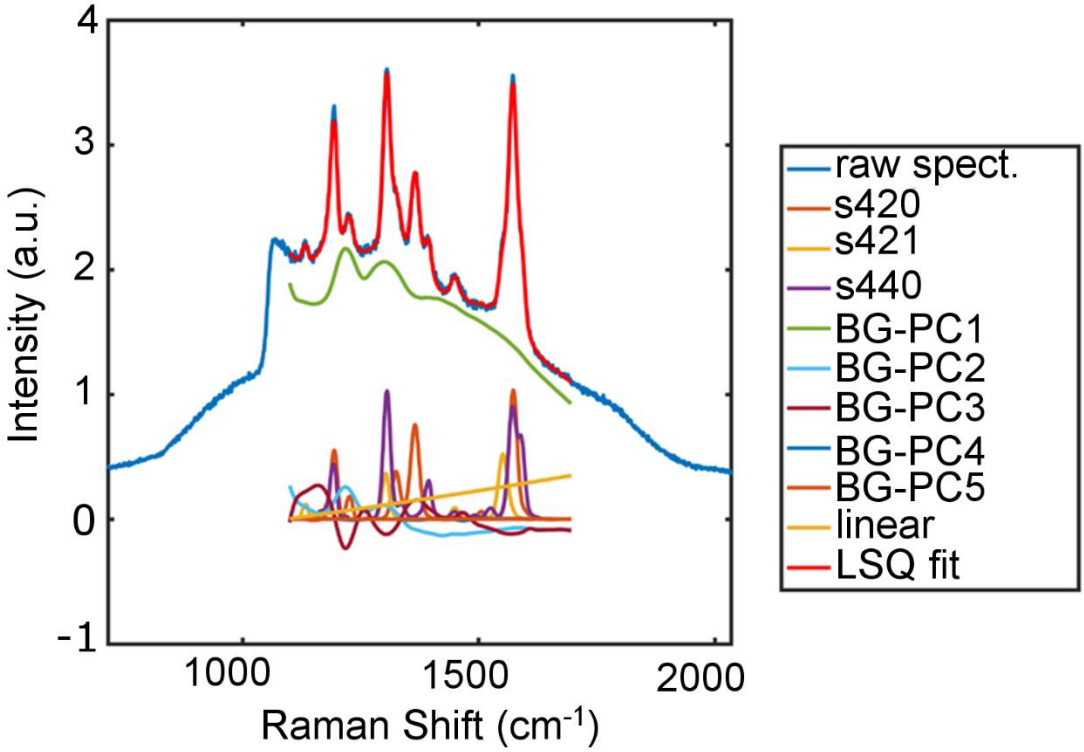

Figure S4: High Resolution Image of Decomposed Raman Spectrum. The blue spectrum spanning the whole spectral window is the raw Raman data. The red data spanning 1100-1700cm^{-1} is the least squares fit to the raw spectrum. All other lines are the decomposed spectral components of b (Equation 1). In the legend, BG-PC stands for background principle component. Details of unmixing are described in the methods section "Spectral unmixing and background subtraction of raw Raman spectra".

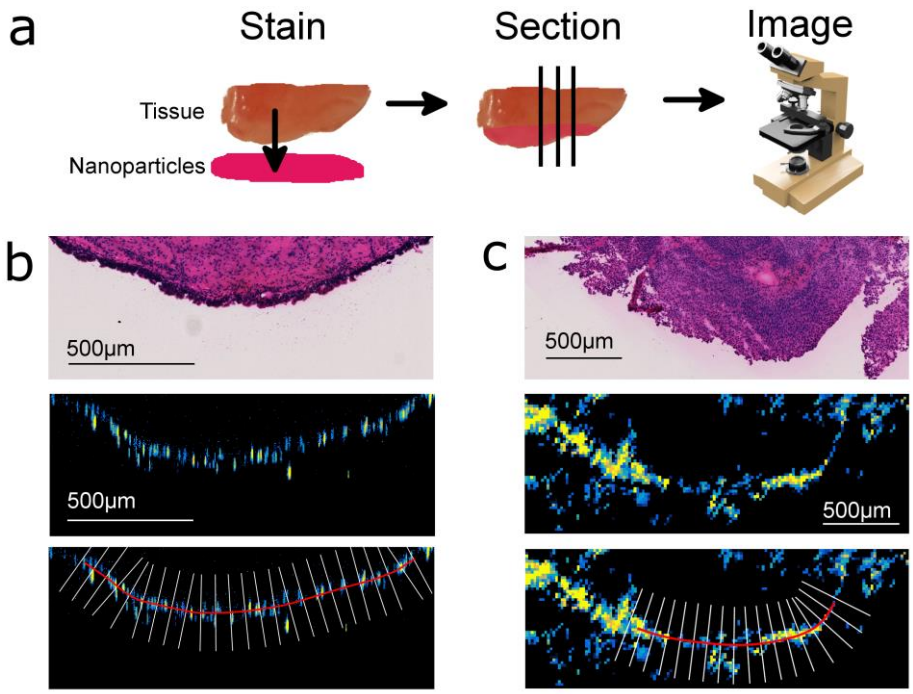

Figure S5: Details of Passive Penetration Microscopy Experiments. a) Experimental workflow. First, ex vivo human tissue samples were stained topically with 1:1:1 ratio of passive, CD47, and CA9-targeted nanoparticles. Second, tissue samples were embedded in OCT, frozen, and sectioned orthogonally to the tissue surface. Finally, adjacent slides were either mounted on quartz slides and imaged on a Raman microscope (5μm by 5μm step size) or stained with hematoxylin and eosin and imaged on a white light microscope. b) sample normal tissue H&E image (top), s421-IgG4 Raman image (middle) and image profiles (bottom) for penetration depth analysis. For the image profiles, the red line was drawn manually and the white lines indicate the computer-generated image profile locations orthogonal to the tissue surface. c) H&E (top), s421-IgG4 (middle), and image profiles (bottom) for a cancerous tissue specimen.

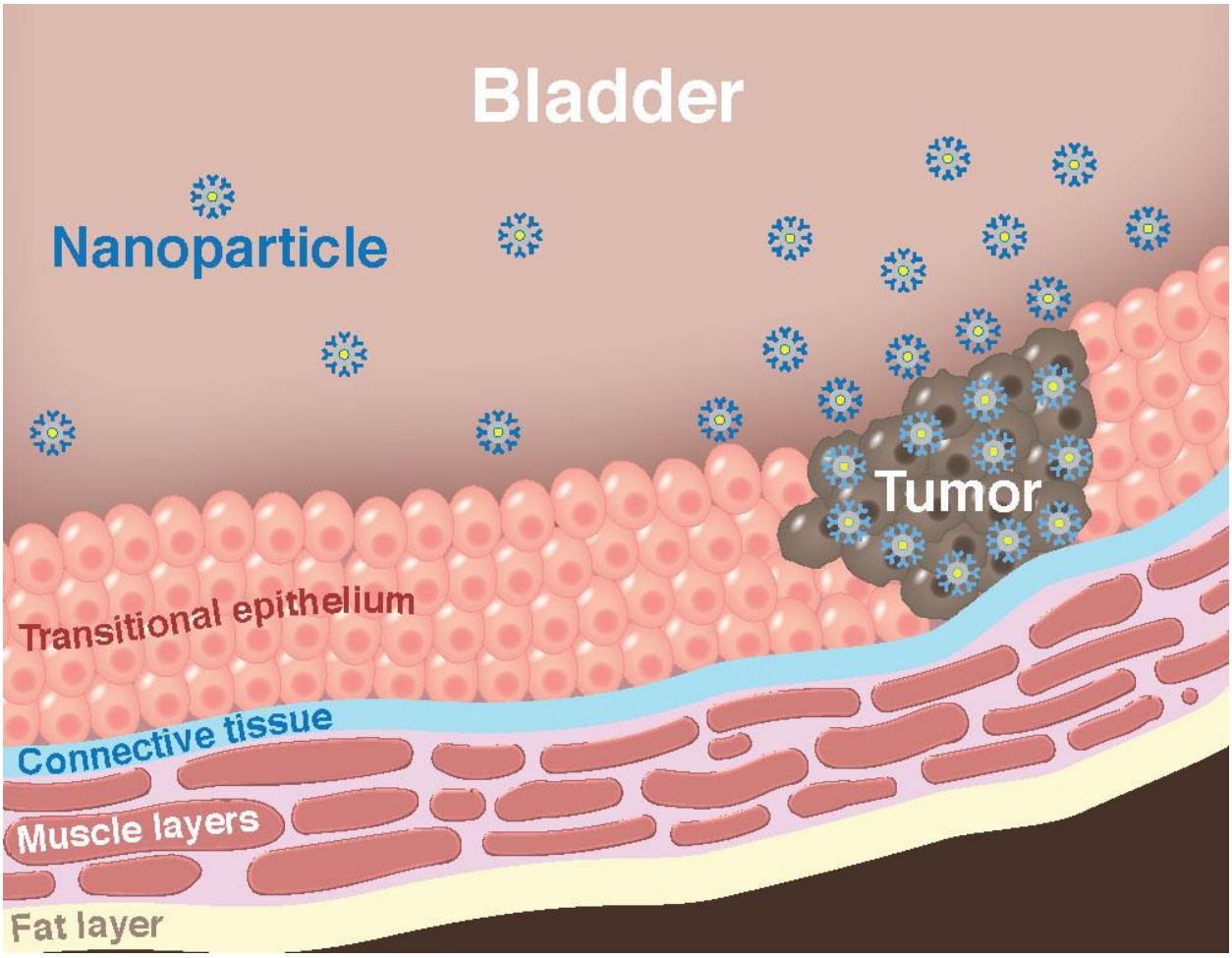

Figure S6: Illustration of the Enhanced Surface Permeability and Retention Effect. Disruption of the transitional epithelium by the tumor resulted in enhanced permeability of bladder to intravesical nanoparticles.

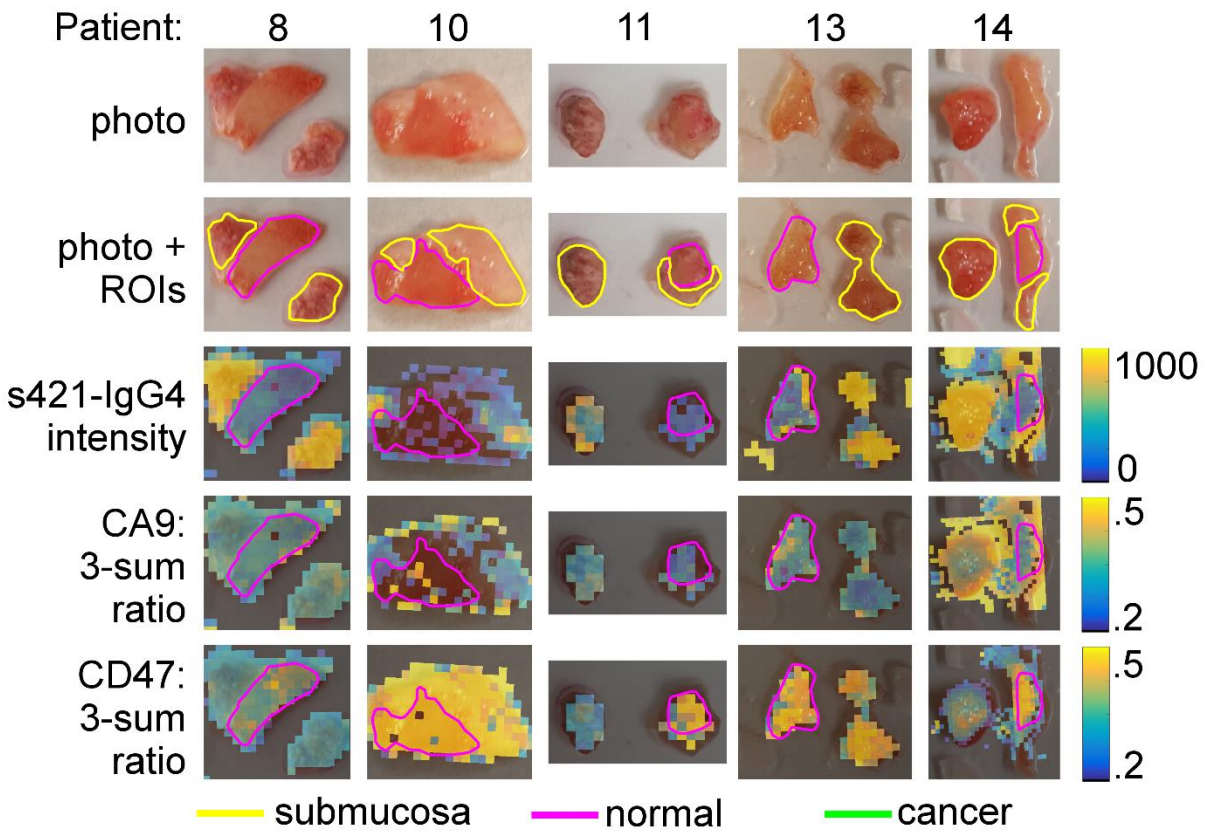

Figure S7: Part 1 of Full Image Dataset. Each column is a different patient and each row is a different type of image. Row 1) photograph of tissue sample. Row 2) Photograph with regions of interest (ROI) superimposed. ROIs are color-coded by tissue type with submucosa as yellow, normal as magenta, and cancer as green. Row 3) s421-IgG4 intensity overlaid on photograph. Row 4) CA9:3-sum ratio overlaid on photograph. Row 5) CD47:3-sum ratio overlaid on photograph. For rows 3-5 only the cancer and normal ROIs are shown because only those ROIs were used in subsequent analysis. In the overlaid images (rows 3-5) images were thresholded based on s421-IgG4 or BG-PC3. All pixels that fell below the threshold or were below the lower colorbar limit were colored black in the overlaid Raman image.

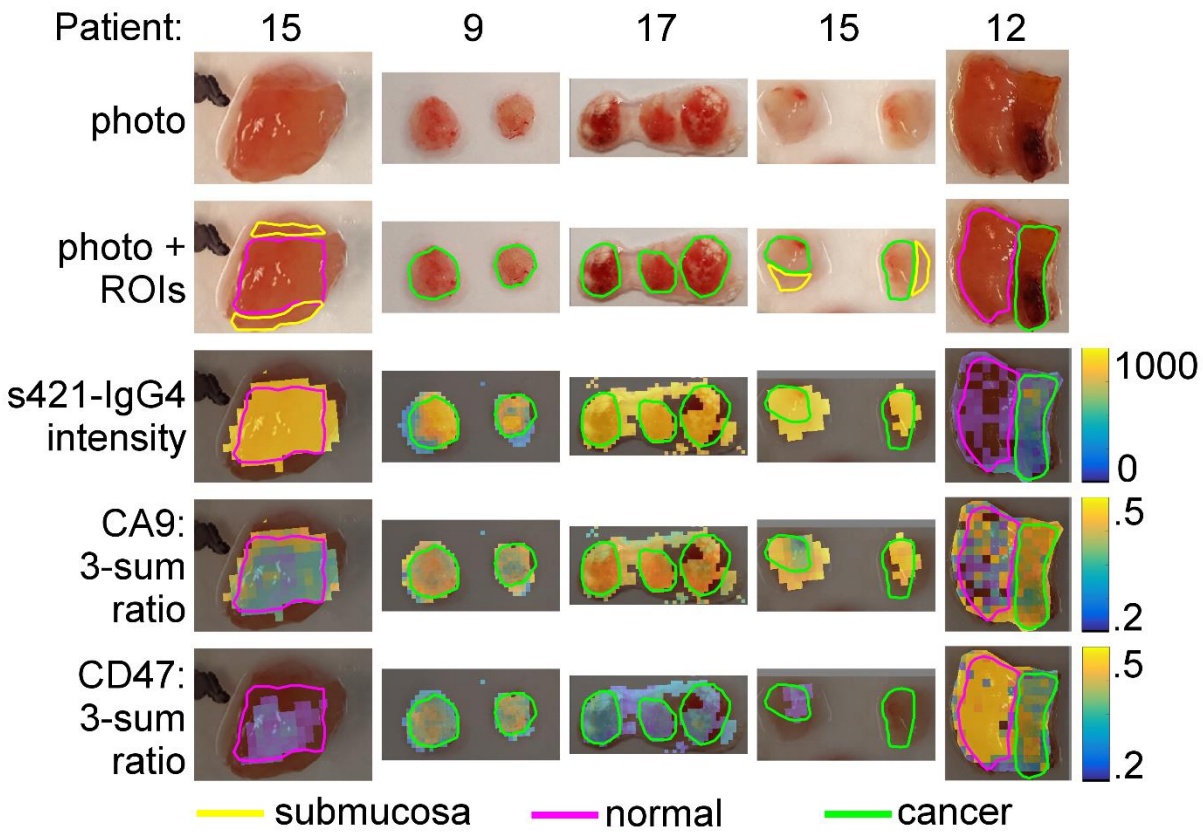

Figure S8: Part 2 of Full Image Dataset. See caption for Figure S7 for details on this figure.

Table S1: Clinical Data for Bladder Tissue Samples

Subject Number	Procedure	Clinical Pathology Results	Used for Microscopy	Used for Endoscope	Other notes
1	Cystoprostectomy	LG pT2a pN0			*
2	TURBT	LG pTa			*
3	TURBT	HG pT1			*
4	TURBT	LG pTa			*
5	TURBT	HG pT1			*
6	cystectomy	pTis pN0			*
7	TURBT	HG T1			*
8	Robotic Surgery	pT3b pN0		n	
9	TURBT	HG pT1		t(x2)	
10	Cystectomy	HG pT3a N0		n	
11	Cystectomy	HG pT4aR1 N0		n	
12	Cystectomy	HG pT3b N2.		n,t	Sarcomatoid differentiation
13	Cystectomy	pT0, N0		n	
14	Cystectomy	HG pT2b N0	n	n	Small cell carcinoma
15	Cystectomy	HG ypT3a pN1		n,t (x2)	Micropapillary and nested variant
16	TURBT	HG pT2			excluded because of excessive cauterization
17	TURBT	HG pTa	t	t (x3)	
18	TURBT	LG pT1a	n,t		
19	TURBT	HG T2	n,t		

* These samples were used for development and optimization of the nanoparticle synthesis and staining procedure, and the results were not included in the manuscript.